APPLIED CATALYSIS B: ENVIRONMENTAL 163 (2015) 424–435

doi:10.1016/j.apcatb.2014.08.022

New copper/GO based material as an efficient oxygen reduction catalyst in an alkaline medium: The role of unique Cu/rGO architecture

Conchi O. Ania[2], Mykola Seredych[1], Enrique Rodriguez-Castellon[3], and Teresa J. Bandosz[1*]

[1]The City College of New York

160 Convent Avenue, New York, NY 10031 (USA)

[2]Dpt. Chemical Processes in Energy and Environment, Instituto Nacional del Carbón (INCAR, CSIC), C/ Francisco Pintado Fe 26, Oviedo 33011 (Spain)

[3]Dept. de Quimica Inorganica, Universidad de Malaga (Spain)

[*]Corresponding author. Tel: (212) 650-6017; Fax: (212) 650-6107; E-mail address: tbandosz@ccny.cuny.edu (T.J. Bandosz)

Abstract

A new hybrid Cu/rGO catalyst obtained by a thermal treatment of the composite of a copper-based MOF with graphite oxide exhibited a marked catalytic activity for oxygen reduction reaction (ORR) in an alkaline medium, high tolerance to methanol oxidation and superior long-term stability over 20 hours. The unique architecture of the copper atoms in the 3D framework of the pristine MOF coupled with the excellent electron transfer properties of rGO lead to materials with a homogenous distribution of copper nanoparticles of specific chemistry assembled within the graphene sheets. Fast O_2 adsorption and charge transfer owing to the strong interactions between copper atoms and graphite oxide resulted in highly stable and active Cu/rGO electrodes, compared to the carbonized MOF. The synergistic effect of copper and rGO in the composite leads to a superior ORR activity in terms of long-term stability and high current densities, close to the best performance reported for Pt and other metal-free electrocatalysts.

Keywords: copper/graphene, composites, surface chemistry, electrocatalysis, oxygen reduction reaction

1. Introduction

Energy related issues are important concerns, which have to be adequately addressed to maintain sustainability of our environment. Since improving the performance of electrocatalysts towards the reduction of oxygen is still a challenge, its optimization remains one of the most investigated electrochemical processes [1, 2]. Triggered by a low tolerance to fuel crossover of Pt/C based cathodes, and the need to lower the cost of devices by using non expensive catalysts, extensive research is being conducted on the development of metal-free catalysts for an efficient oxygen reduction reaction (ORR) under fuel-cell working conditions. Among the materials investigated, doped nanostructured carbons, including graphene-like materials, have become a recent research focus. It has been demonstrated that the combined effect of the heteroatoms doping coupled with the outstanding feature of the graphene material (i.e., high electrical conductivity, high surface area, efficient charge transfer) provides rather stable catalysts with activities close to that of Pt/C cathodes while overcoming the fuel crossover tolerance. Nevertheless, in most cases the ORR follows an incomplete 4 electron pathway [3]. Even though non-precious metal surfaces (i.e., Fe, Co, Mn oxides and nanoparticles) favor the four-electron transfer mechanism, they still cannot be considered as a replacement of Pt in terms of activity [4-6]. An important issue of concern is still the control of the size, shape, composition, structure and homogeneity of the dispersion of the metallic nanoparticles owing to the fact the ORR efficiency strongly depends on all these factors [7]. Recent studies have focused on coupling the best characteristics of non metal oxides dispersed on graphene-like materials, with a resulting nanocomposite showing an enhanced ORR performance compared to its individual components, and close to that of Pt [8-12].

Copper has a rich redox chemistry based on the reduction to Cu(0) and Cu(I), and oxidation to Cu(III) or even Cu(IV), with many oxidative reactions being catalyzed by different copper

complexes and oxides [13-15]. Compared to the most efficient non-noble metal ORR catalysts, copper typically displays a low reactivity and easily undergo corrosion under certain electrolytes [16]. However, copper based enzymes are known of oxygen reduction activity. A well-known example is laccase, a multicopper oxidase that catalyzes the four-electron reduction of oxygen to water at overpotentials lower than those of noble metals [17, 18]. Furthermore, recent studies have also reported a promising performance of CuO/Gr composites for ORR [9, 19]. Knowing the oxygen reduction capability of copper and aiming at improving the mentioned above drawbacks (low activity and stability), we have selected copper as a low-cost non-precious catalytic metal. We try to imitate/replicate the high oxygen reduction activity of multicopper active sites in natural systems by producing a synthetic carbon-based matrix with deposited copper species. Therefore the objective of this paper is to present the excellent performance of a new hybrid ORR catalyst obtained from the composite of Metal Organic Frameworks (MOF) with graphite oxide (GO) [20]. The MOF/GO composites were synthesized previously with an intended application in the separation of toxic industrial gases from air [20-22] and in sequestration of CO_2 [23]. Even though they have been proven to have an excellent performance, there is an issue with their long-term stability when exposed to atmospheric moisture. Therefore the carbonization and reuse of a "non-so-active" composite might be an attractive materials' recycling path. The application of MOF in electrocatalysis has been scarcely explored, due to their intrinsic poor electron conductive properties and limited charge transfer [19, 24, 25]. Some attempts to partially overcome this limitation have considered hybrid MOF composites prepared by adding a conductive phase; for instance, Jahan and co-workers [19, 26] have recently reported a graphene oxide/Cu-MOF [19] and graphene-porphyrin MOF [26] composites with enhanced electrocatalytic properties for ORR and hydrogen and oxygen evolution reactions. Still these materials underperform the activity of Pt based catalysts [10, 27, 28]. Another MOF, Co-based imidazolate framework, was used as a carbonization precursor for ORR catalysts by Ma

and coworkers [29]. The observed catalytic activity was linked to the coordination of cobalt with nitrogen owing to the specific chemistry of the organic linkages. In our approach we use materials derived by heat treatment of copper-based MOF, HKUST-1, and a HKUST-1/graphite oxide (GO) composite [20] as electrocatalysts for ORR in an alkaline medium. The presence of the GO phase in the composites results in specific chemical linkages with the MOF units. A heat treatment (HT) of the composite at 800 ºC resulted in unique surface features of the catalyst owing to the specific spatial location/distribution of graphene units [20, 23], to their binding with MOF, to the reducing character of the carbon component, and to an enhanced electrical conductivity. This synthetic route also overcomes the usual problems encountered with the preparation of metal-doped carbons, regarding dispersion and aggregation of the metallic particles. Furthermore, the highly distributed and partially reduced GO (rGO) directly connected with a copper catalyst phase is expected to enhance an electron transfer within the catalyst matrix. To stress the importance of the specific chemical and structural nature of the composite precursor (with 50 % GO) the surface features and the performance of the new catalyst (CMGr) are compared to those of a catalyst obtained by heat treatment of MOF itself (CM).

2. Experimental

2.1. Materials

The preparation of the copper based MOF, HKUST-1 [30], graphite oxide (GO) and their composite with 46 wt.% of GO has been addressed in details previously [20]. The large amount of GO in the composite was targeted to provide a good electrical conductivity in the resulting catalysts. Briefly, GO powder (64.7 mg_{GO}/mL DMF) was added to a mixture containing the MOF precursors well-dissolved in DMF, sonicated for 5 min, and stirred for another 30 min. The suspension was then transferred to a flask and heated at 85 ºC in an oil bath for 21 h under continuous shaking. After cooling, the crystals were filtered, washed and

immersed in dichloromethane for 3 days, and dried at 170 ºC under vacuum for 28 h. Subsequently, the samples were heated under an inert atmosphere at 800 ºC (100 mL/min for 1 hour and 10 ºC/min); the heat treated HKUST-1 and MOF/GO samples are referred to as CM and CMGr, respectively. This process was expected to result in a total collapse of the initial materials' ordered porous structure and lead to a development of new porosity of a disordered nature. The performance of the samples was compared to that of a commercial Pt/C catalyst (20 wt. % Pt on Vulcan XC-72, dp < 5 nm for Pt, Sigma-Aldrich).

2.2. Methods

2.2.1. Electrochemical Characterization

The performance of our materials for electrochemical ORR was investigated in 0.1 M KOH using a three-electrode cell with Ag/AgCl/KCl (3 M) as a reference electrode. The measurements of cyclic voltammetry and chronoamperometry were carried out on VersaSTAT MC (AMETEK, Princeton Applied Research) with a scanning rate of 5 mV/s (cyclic voltammetry). The working electrode was prepared by mixing the active material with polyvinylidene fluoride (PVDF) (9:1) in N-methyl-2-pyrrolidone (NMP) until homogeneous slurry. The slurry was coated on a Ti foil (current collector) with the total surface area of 1 cm^2 of an active material. To evaluate the stability of the electrodes, they were initially stabilized under N_2 or O_2 saturation in the electrolyte in the potential range of 0.19 to -0.8 V at a scan rate of 5 mV/s. Linear sweep voltammograms were obtained in 0.1 M KOH using 757 VA Computrace (Metrohm) at various rotation rates (from 0 to 2000 rpm) with Ag/AgCl (3 M KCl) and a Pt wire as a reference and a counter electrode, respectively. The working electrode was prepared by dispersing 2 mg of the catalyst in 1 ml of deionized water and 0.5 ml of 1 wt.% Nafion aqueous solution. About 5 µl of the prepared slurry was dropped (three times) on a polished glassy carbon electrode (Metrohm, Switzerland, diameter 2 mm) and dried at 50 ºC in air. The potential was swept from 0.19 to -0.8 V at a scan rate of 5 mV/s.

After each scan, the electrolyte was saturated with O_2 for 20 minutes using air as a supplier. All the experiments were carried out at a room temperature.

The concentration of dissolved oxygen in the electrochemical cell was measured using an oxygen sensor (LDO101 HACH Company, Model – HQ440d) immersed in the electrolyte.

2.2.2. X-ray diffraction (XRD)

XRD measurements were conducted using standard powder diffraction procedures analyzed by $Cu_{K\alpha}$ radiation (tension – 40 kV and current – 40 mA) generated in a Phillips X'Pert X-ray diffractometer. The scan rate used was 2.3 deg/min.

2.2.3. Scanning electron microscopy (SEM)

SEM images were performed at Zeiss Supra 55 VP. The accelerating voltage was 5.00 kV. Scanning was performed in situ on a sample powder without coating. Electron-dispersive X-ray spectroscopy (EDX) analysis was done at magnification 10 KX and the content of elements on the surface was calculated.

2.2.4. Transmission electron microscopy (TEM)

TEM was performed on a Zeiss EM 902 instrument. The microscope has a line resolution of 0.34 nm and a point resolution of 0.5 nm and operates in normal diffraction, and low dose modes at 50 or 80 kV. Analyses were performed after the samples were dispersed in ethanol.

2.2.5. Evaluation of porosity

Sorption of nitrogen at its boiling point was carried out using ASAP 2020 (Micromeritics, Surface Area and Porosity Analyzer). Before the experiments, samples were out-gassed at 120 ^{o}C to constant vacuum (10^{-4} Torr). The surface area, S_{BET}, (Brunauer-Emmet-Teller method was used), the micropore volume, V_{mic}, (calculated using the Dubinin-Radushkevich approach) [31] the mesopore volume, V_{mes}, the total pore volume, V_t, (calculated from the last point of the isotherms based on the volume of nitrogen adsorbed). The volume of mesopores, V_{mes}, represents the difference between total pore and micropore volume. The relative microporosity was calculated as the ratio of the V_{mic} and V_t.

2.2.6. Adsorption of water and benzene

The hydrophobicity level of our samples was determined comparing their affinity to adsorb water and benzene. Predetermined amounts of dry samples were exposed either to water or benzene vapours in air-tight environments for 24 hours at room temperature. The amounts adsorbed were measured gravimetrically. The hydrophobicity level (HL) is defined as the ratio of the amount of benzene adsorbed to that of water.

2.2.7. X-ray photoelectron spectra (XPS) analysis

XPS analysis were collected using a Physical Electronics PHI 5700 spectrometer with non-monochromatic Mg K_α radiation (300 W, 15 kV, 1253.6 eV) for the analysis of the core level signals of C 1*s*, O 1*s* and Cu 2*p* and with a multichannel detector. Spectra of powdered samples were recorded with the constant pass energy values at 29.35 eV, using a 720 μm diameter analysis area. Under these conditions, the Au $4f_{7/2}$ line was recorded with 1.16 eV FWHM at a binding energy of 84.0 eV. The spectrometer energy scale was calibrated using Cu $2p_{3/2}$, Ag $3d_{5/2}$, and Au $4f_{7/2}$ photoelectron lines at 932.7, 368.3, and 84.0 eV, respectively. During data processing of the XPS spectra, binding energy values were referenced to the C 1*s* peak of PVDF (carbon atom bond to fluorine as marked by the asterisk in the formula: $-CH_2-C^*F_2-$) at 290.6 eV [32]. The PHI ACCESS ESCA-V6.F software package was used for acquisition and data analysis. A Shirley-type background was subtracted from the signals. Recorded spectra were always fitted using Gauss–Lorentz curves, in order to determine the binding energy of the different element core levels more accurately. The error in BE was estimated to be ca. 0.1 eV. A first acquisition was performed with 8 min of irradiation time only to avoid as much as possible the photo-reduction of Cu(II) species. Nevertheless, a Cu(II) reduction in high vacuum during the analysis cannot be excluded [33].

2.2.8. DC conductivity measurements

The DC conductivity was measured using a 4-probe method on the pellets with the composition 95 wt. % of copper/GO based materials and 5 wt. % polytetrafluoroethylene as

binder. The prepared composition was pressed by a Carver Press machine applying 2 tons pressure and a disk-shaped well-packed pellets with diameter 8 mm were formed. The pellets were dried in oven for 12 hours. The pellets' thickness was measured by a spring micrometer. The measurement of conductivity was carried out using the Keithley 2400 multimeter.

3. Results and discussion

3.1. Characterization of Cu/rGO hybrid materials

The SEM and TEM images of the catalysts indicate a marked difference between both samples' textures (Figure 1 a-l). The carbonized MOF (sample CM) shows a highly heterogeneous structure with light areas corresponding to a carbon phase and dark metallic globular particles or aggregates of a different chemical nature (Figure 1 c,d). The latter have sizes of about 20 nm (Figure 1 i-l). The EDX analysis indicates that they consist of mainly copper metal (Table S1). In CMGr (Figure 1a,b), globular copper-containing particles are also seen on the carbonized MOF particles. Interestingly, the particles here preserved the shape of MOF crystals (Figure S1; ESI) indicating the constraining effects of the GO layers resulting in the preserving the shapes of the original MOF crystals in their carbonized phase. The graphene phase seems to be mainly separated from the MOF-origin phase and large aggregates can be easily distinguished. Besides this, some corrugated graphene layers are directly covered with thin layers of the aggregated copper particles (Figure 1 e-h). The latter are more heterogeneous in their sizes on the surface of CMGr than those on CM and the EDX analysis indicates that the largest particles are mainly metallic copper, whereas in the smaller ones oxygen can be also detected. An EDX mapping also shows that the surface of CMGr is much more heterogeneous than that of the CM sample (Table S1; ESI). Of significance might be the presence of copper particles growing on the layers of rGO and the marked surface heterogeneity of this material. The differences in the content of carbon and copper on the surface follow the trend in the composition of the precursors.

Information on the materials' structure and chemistry was obtained from thermal analysis (Figures S2 and S3, ESI), XRD (Figure 2) and XPS (Figure 3). The thermal profiles in air indicated 92 % and 57 % ash/ an inorganic matter in CM and CMGr, respectively. The difference in the ash content is in agreement with the differences in the content of the combustible carbon based material in the samples [20]. A visible increase in the mass of the samples at about 200 ^{o}C is linked to the oxidation of copper [34]. That increase is about 5 % for CMGr and 2 % for CM suggesting that copper in the former sample is more reactive in air than that in the latter sample, even though the total copper content is about 50 % smaller. DTA curves (Figure S2c; ESI) clearly show the exothermic effects related to the formation of oxides and carbon phase burning. A sharp peak at 270 ^{o}C for CMGr suggests the rather chemically homogenous nature of reduced copper species on this material. On the surface of CM the majority of copper is oxidized at 200 ^{o}C. When the analysis was run in helium both materials revealed similar thermal fingerprints, with a small mass loss (ca. 1.5 wt.% in both cases) between 300-500 ºC due to the CO_2 evolution from the decomposition of copper carbonates formed from the organic linkers of MOF (Figure S3; ESI).

Both catalysts also exhibit rather similar diffraction patterns, being the consequence of the destruction and chemical transformation of MOF during the heat treatment (HT) at 800 ^{o}C. The carbonization temperature was chosen based on the observed thermal stabilization of pristine materials (Figure S4; ESI) and the expected reduction of a significant amount of carbonyls and OH groups of GO [35]. The XRD pattern of CMGr shows sharp peaks at 44 and 52º assigned to metallic copper, and a small peak attributed to Cu_2O. Since the oxidation state of copper in HKUST-1 is (+2) and both materials present the similar copper diffraction patterns, the reductive atmosphere is provided not only by GO but also, to some extent, by the pyrolytic carbon phase formed during the decomposition of the organic linkers of MOF. The

crystallite size of metallic copper estimated using the Scherrer equation [36] is 20.6 nm for CM and 27.4 nm for CMGr. This difference follows the trend observed for the size of copper particles seen on the SEM images (Figure 1a-d). Thus, the insertion of GO in the MOF framework during the synthesis modifies the chemical environment of the copper atoms, causing an aggregation in slightly larger cluster/nanoparticles during the HT. The XRD peaks are also sharper for CMGr, indicating a higher level of crystallinity. A well-defined sharp peak at $2\theta = 26^{\circ}$, characteristic of a high order stacking of graphene layers (002) is clearly visible on the XRD pattern of CMGr. The absence of the peak at $2\theta = 9.3^{\circ}$ corresponding to the pristine GO [20] demonstrates that this phase is reduced during the HT (rather than undergoing exfoliation/expansion) to form reduced rGO aggregates, as seen on the SEM/TEM images. This contrasts with the results recently reported by Zhou and co-workers, where the peak of the ordered stacking of graphene sheets was not detected on a CuO/N-rGO composite [9].

Furthermore, a twice larger porosity found for CM (Table 1) than that for CMGr suggests that the agglomerates of rGO do not provide any porosity (beyond a "dilution" mass effect). It has to be stressed here that the porosity of the materials addressed in this paper is much smaller than that for the MOF/GO composites and MOF itself described in details by Petit and coworkers [20]. This is related to the chemical changes occurring during the thermal treatment at 800 ºC. As seen in Figure S4 (ESI) the organic linkers present in MOF itself or the MOF/GO composites decompose at 330 ^{o}C. Since the linkers are the structural units building the porous structure of the initial MOF, their decomposition results in the collapse of the materials' porosity.

The details on the chemical composition of the prepared catalysts and on the form of copper are provided by XPS analysis. The atomic concentration of elements on the surface is listed in Tables 2 and 3. Given the composition of the precursors, we attribute the trace amount of

nitrogen detected by XPS to the NMP solvent used to fabricate the electrodes and we do not link it to the observed catalytic activity. The charge corrections of the spectra were done against carbon atom marked with an asterisk (*) of PVDF -(CH_2-C*F_2)- at 290.6 eV [32] due to the complex nature of the C 1*s* spectra, where the correction with the adventitious carbon is not possible.

The C 1*s* core level spectrum of sample CMGr was deconvoluted to six contributions (Figure 3 and Table 3). The intense peak at 284.6 eV was assigned to carbon in sp^2 configurations, and the contributions at 287.1 eV and 288.4 eV were assigned to carbonyl and carbonates or carboxylic groups, respectively [37, 38]. The low intensity peak at 282.4 eV is assigned to the possible presence of copper carbide [39, 40]. The contribution at 286.1 eV is mainly due to carbon atom C* from PVDF -(CH_2-C*F_2)- [32] and, in a minor extent to the presence of phenolic and other C-OH groups in addition to C-O-C from ether bonds [32]. As expected, for both samples the percentage of this contribution was more or less similar to that of carbon C* of PVDF -(CH_2-C*F_2)- at 290.6 eV. Indeed, the F 1*s* signal appeared at 688.0 eV for both materials, in agreement with the value reported for PVDF [32].

As seen in Table 3, the main differences in the C 1*s* core level spectra between two samples studied are in the presence of copper carbide in CMGr (not detected in sample CM) and in the contribution of pyrolytic and graphitic carbon. For CM sample pyrolytic carbon is predominant over the graphitic structures, which is in agreement with the amorphous carbon phase observed in the TEM images (Figure 1 i-l). It is linked to the decomposition of the MOF organic linkers. In the case of CMGr, the graphitic carbon is the dominant phase (ca. seven times more than in CM), due to the incorporation of the rGO layers to the composite. In addition, both samples exhibit the similar distributions of carbon atoms in different oxygen environments (accounting for carbonyl, carbonates or carboxylic groups). This was further

confirmed by the O 1*s* core level signals; the broad peaks were deconvoluted to three contributions at 530.8 eV 531.7 eV and 533.5-533.8 eV assigned to oxygen from metal oxides, carbonyl/carboxyl and phenol groups [32, 38], respectively (Figure 3). On the surface of CM there is more oxygen at a low energy contribution, which suggests that more copper is in the oxidized form than that in CMGr.

The Cu 2*p* core level spectra for samples CMGr and CM are noisy but it is possible to analyze them. The main Cu $p_{3/2}$ signal is composed of two contributions at 932.9 and 935.2 eV, where the former is assigned to surface Cu(0) and the latter to Cu(II) [41]. The ratio of the areas of the satellite region between and the area of the main Cu $2p_{3/2}$ signal (Cu $2p_{3/2}$sat/Cu $2p_{3/2}$mp) is indicative of the reduction degree of copper. When only Cu(II) species are present, this ratio would be 0.55, and we have found values of 0.36 and 0.33 for CMGr and CM, respectively. The Cu $2p_{3/2}$sat/Cu $2p_{3/2}$mp is 0.36 and 0.33 for CMGr and CM, respectively, indicating an important reduction degree of surface copper. The assignment of the chemical state of reduced copper is not easy because the Cu $2p_{3/2}$ components for Cu(I) and Cu(0) are very similar. To solve this ambiguity, the Auger's modified parameter (α') was determined (Figure S5; ESI) using equation (1)

$$\alpha' = \text{BECu } 2p_{3/2} - \text{BECuLMM} + h\nu \quad (1)$$

where BECu $2p_{3/2}$ is the binding energy of the contribution Cu $2p_{3/2}$, BECuLMM the binding energy of the Auger signal CuLMM and $h\nu$ the energy of the incident radiation (1253.6 eV) [32]. The α'values for CMGr are 1849.8 and 1848.3 eV. The former is assigned to Cu(0) and the latter to Cu(II) on the sample surface. In the case of sample CM, the α'values are 1849.5 and 1848.3 eV, respectively. Thus the data shown in Wagner plot (Figure S5; ESI) suggests that both Cu(0) and Cu(II) are present on the surface of our catalysts.

Summarizing, the surface chemical composition (in atomic concentration %) determined by XPS (Table 2) indicates that sample CMGr presents a higher concentration of carbon and lower concentration of oxygen and copper than those on CM. In order words, the surface of sample CM is more oxidized and contains a higher amount of copper. Also, based on the ratio of the pyrolytic to graphitic carbon in both materials, it is clear that the CM sample has a much smaller surface concentration of a carbonaceous conducting material. The combination of the conducting carbonaceous phase and the well-dispersed copper particles in a metallic state formed during pyrolysis/reduction of Cu-based MOF is expected to create a specific fast electron transfer environment in sample CMGr, which would enhance ORR. These features are expected to create hydrophobic sites that favor the adsorption/withdrawal of dissolved oxygen from water.

3.2. Electrochemical performance in alkaline solution

Prior to ORR measurements, the electrochemical behavior and stability of the obtained materials was investigated by cyclic voltammetry (CV); comparative studies were performed on samples CMGr and CM in 0.1M KOH at various potential ranges (all potential values are referred vs. the Ag/AgCl/KCl (3 M) reference electrode). The electrochemical response of pristine HKUST-1 could not be measured since this material is unstable in moist air [42] and collapses when immersed in aqueous electrolytes (data not shown). On the other hand, the electrochemical response of rGO has been discussed elsewhere [11, 43]; the outcome of these previous studies is used here only for a data interpretation and to indicate the importance of the surface features of the composites addressed in this paper.

The stability of the electrodes was first investigated by running several consecutive cycles under oxygen (sO) or nitrogen (sN) saturation of the electrolyte (Figure 4). In both cases the first cycle started from the open circuit potential (ca. -0.24 V) in the cathodic direction and no

redox peaks were detected; under the reverse (anodic) sweep, the waves corresponding to oxidation of copper become visible. This indicates that most of the copper in the initial materials is in its elemental state, which is in agreement with the XRD patterns (Figure 2). Furthermore, the intensities of all peaks increase upon cycling indicating that the materials are electrochemically stabilized during the scans. After 30 cycles, the constant intensity was recorded and the materials were considered as fully stabilized.

When the electrodes were stabilized in the electrolyte saturated with nitrogen (series sN), two redox peaks (A1, A2) due to Cu(0)/Cu(I)/Cu(II) transitions were revealed in the anodic sweep. Peak A1 corresponds to the oxidation to Cu(I) (r.1) and peak A2 is related to the formation of Cu(II) species (oxides/hydroxides) [44, 45] following either a one (i.e., Cu_2O to Cu(II) as in r.2) or two step reaction (direct Cu to Cu(II) as indicated in r.3 and r.4). Higher oxidation states of copper were not detected since the potential cut-off was hold below 0.6 V [45-47]. In the cathodic sweep, two peaks C1 and C2 are visible on the CV curves before hydrogen evolution, corresponding to the reduction potential position of peaks A1 and A2. The high intensities of C1 and A2 peaks suggest that a direct Cu(0)/Cu(II) transition (r.3 and r.4) is a predominant reaction on CMGr-sN.

$2Cu + 2OH^- \rightarrow Cu_2O + H_2O + 2e^-$ pair A1/C1 (r.1)

$Cu_2O + 2OH^- \rightarrow 2CuO + H_2O + 2e^-$ pair A2/C2 (r.2)

$Cu + 2OH^- \rightarrow CuO + H_2O + 2e^-$ pair A2/C2 (r.3)

$Cu + 2OH^- \rightarrow Cu(OH)_2 + 2e^-$ and then $Cu(OH)_2 \leftrightarrow CuO + H_2O$ (r.4)

The intensities and positions of the redox peaks are about the same for CM and CMGr, regardless the stabilization conditions, indicating that the peaks are attributed to the same copper transitions. However, the voltammograms of CM are clearly more resistive (Figure 4)

due to the limited charge transport in the absence of the rGO phase. The cathodic potentials agree with those reported for the anodic oxidation of copper in alkaline solution [45, 46]; in contrast, the anodic waves are shifted to more positive potentials, likely as a consequence of the different chemical environments of the copper atoms in these materials.

When the stabilization of the electrodes was performed in oxygen (series sO), differences became evident in the shape and the intensity of the voltammograms. The potential positions of the pair A1/C1 are -0.27/-0.82 V, and those of A2/C2 are -0.11/-0.48 V for CMGr-sO, whereas those of CM-sO remained close to those of the samples stabilized under N_2 (Figure 4b). The cathodic shift in the position of peak A2 potential in CMGr-sO suggests that different Cu(II) species are formed upon stabilization in the presence of oxygen (following reactions r.2, r.3 and r.4) than those without oxygen in the system. The intensity of the peaks is also altered; cathodic peaks C1 and C2 are more intense than anodic peaks, as usually observed for copper electrodes that are easily reduced due to its inherent electronic structure [44]. Furthermore, the intensities of C1 and C2 peaks become similar, suggesting that the direct Cu(0)/Cu(II) transition is no longer predominant (as for the stabilization in nitrogen) but rather the two step process is favored (r.2 and r.1). It is important to mention that no leaching of copper from the surface of the electrodes was detected in 0.1 M KOH during the stability testing.

To evaluate the role of the dissolved oxygen during the stabilization of the electrodes, experiments were also conducted under controlled aeration conditions of the electrolyte (providing initial O_2 saturation -ca. 8.9 mg/L- but preventing extra supply during consecutive runs). The amount of dissolved oxygen in the electrolyte decreased sharply (ca. 4.7 and 3.1 mg/L for CM and CMGr, respectively) during cycling (Figure 5) indicating that the oxygen reduction reaction occurs simultaneously during the cyclic stabilization of the electrodes in

the presence of oxygen. This process modifies the distribution of the copper species on the surface of the material as revealed in the changes in the shape (and intensity of the waves) of the voltammograms (Figure 4b), as mentioned above. This effect cannot be attributed to the polarization of the electrodes, as it was not observed upon the stabilization under the nitrogen atmosphere (series sN); we did not observe any change either upon exposure to oxygen (neither from atmosphere or in the electrolyte) thus it has to be related to the simultaneous occurrence of the ORR itself and hence the formation of intermediates. After 1000 cycles, the material still showed a large activity towards the ORR, as discussed below. This process was visible in spite of the low oxygen saturation conditions of our electrolyte (ca. 8-9 mg/L due to the use of air as oxygen supply), hence measured ORR currents are much lower that those determined at higher oxygen saturation conditions (ca. 36 mg/L attained with O_2 purging) [48].

Due to the complex electrochemical behavior of the prepared materials, with partially overlapping of the copper redox reactions with the potential of ORR, it becomes difficult to establish if the observed ORR is a copper- mediated process. To gain an additional insight on the process, linear sweep voltammetry (LSV) on a modified rotating disk electrode (RDE) was recorded at different rotating speeds from 0 to 2000 rpm (Figure 6a). Figure 6b shows the CV corresponding to the materials casted on a glassy carbon electrode after the electrochemical stabilization (both sN and sO series), where the electrocatalytic activity for ORR of our materials is clearly evidenced when comparing the signals in the presence and absence of dissolved oxygen. The cathodic background current measured in CMGr (both -sN and -sO) in O_2-free electrolyte at 0 rpm shows a stationary current from 0.2 to -0.2 V, followed by the waves corresponding to the reversible redox transitions of copper at more negative potentials. The onset potential of these copper cathodic waves is more negative than the onset of the ORR in all the samples, as clearly seen in Figure 6b (inset). Despite the

complex redox chemistry of our catalysts, this allows to distinguish between the two electrochemical processes, and hence to confirm the electrocatalytic activity of the tested materials for ORR. Also, as seen in Figure 6a, the intensity of the background current (measured in O_2-free electrolyte at 0 rpm) is 2-3 times lower for CMGr-sN than that of CMGr-sO, suggesting that the contribution of copper transitions to the mixed current is much lower for the former sample. For CMGr-sO, the current associated with copper transitions (C1 and C2 peaks) is very high and partially overlaps the mixed current at potentials above -0.4 V, complicating the study of the ORR process in this electrode.

The onset potential for the ORR is an important criterion to evaluate the activity of an electrocatalyst; we have calculated this value as indicated in [49], as the intersecting point of the extrapolation of the linear segments of the voltammetry curves corresponding to the cathodic and background branches (see example in Figure 6a). The corresponding ORR onset potentials for CMGr-sO and CMGr-sN, are -0.140 and -0.150 V respectively; for CM, the onset value at -0.185 V was obtained regardless the stabilization procedure. The values of CMGr are slightly more anodic (between 5-15 mV) than those measured for rGO (Figure 7) [11], showing the enhancing effect of copper. Also, the onset potential is shifted to more positive values for the composite stabilized under oxygen, and it is more anodic for CMGr compared to that for CM, anticipating a better catalytic performance on the composites and corroborating the synergistic effect of rGO. Compared to the results published in the literature, the onset potential values are similar to those reported for CuO/r-NGO [9], Cu-MOF/GO composites [19] and some metal-free doped graphene materials [10], but still less positive than that of Pt/C (Figure 7a and Figure S7 and S8; ESI) [10].

The LSV curves also reveal differences between the synthesized samples. CM-sN and CMGr-sN show an increasing current density pattern as the potential becomes more negative, as

commonly observed for ORR catalysts [10, 11]. The measured current for CMGr-sN is 3 to 4 times higher than that for CM (both sN and sO), indicating the better performance of the former sample. This is more clearly seen in Figure 7 showing the comparison of the performance of both CMGr samples with that of a commercial Pt/C catalyst (20 wt. % Vulcan Pt/C) and rGO measured under the same experimental conditions (air as oxygen supply). The current density values for the CMGr-sN are also close to the best performance reported for Pt (21 mA/cm^2) and some graphene-based metal free catalysts [10] and outperforming other Cu-based catalysts [9].

On the other hand, the LSV curves of CMGr-sO show an unusual pattern (still following a somewhat increasing trend with the rotating speed), due to the overlapping of the intense reduction waves corresponding to copper transitions. Owing to the pronounced effect of these waves and the large background current at negative potentials, the mixed current density could be attributed to various overlapping processes, making the assessment of the exact role of copper (if any) in the ORR difficult. To analyze the electrochemical behavior of CMGr-sO two different regions can be distinguished. At potentials between -0.2 and -0.4 V, the electrocatalytic activity of this sample is clearly seen since the contribution of ORR can be unambiguously isolated from that of the copper waves (Figure 6b, inset). At more negative potentials (from -0.4 to -0.8V), the background current associated to C1 and C2 peaks is very high, largely exceeding and overlapping the hydrodynamic electrochemical response of the electrode when oxygen is introduced to the cell (Figure 6b). As the contribution of ORR to the mixed current recorded in this region is unclear, it was not considered for the calculation of the number of electron transfer.

The Koutecky–Levich (K-L) plots obtained from the LSV at various rotating speeds are collected in Figure 8a. Representative data corresponding to -0.4 V is shown for all four

samples, with the exception of CMGr-sO where calculations are presented at -0.34 V owing to the poor fitting at -0.4 V. Data corresponding to other potentials is shown in Figure S6 (ESI). The electron transfer numbers (n) were calculated from the slopes of the K-L plots and its dependence on the potential is presented in Figure 8b. For CMGr-sO the number of electron transfer is only evaluated up to -0.4 V (as discussed above). As seen, the n values are very low (n = 1-2) for both CM samples, indicating the low electrocatalytic selectivity of the carbonized MOF material. For the composites, the number of electrons transfer increased significantly reaching values close to 4 at -0.34 V for CMGr-sO. In all of them, the n value follows a stable trend with the potential, characteristic of electrochemically stable ORR process, confirming the stability of the electrodes. Since CM and CMGr have similar copper species (Figure 2 and 4), the role of rGO and its contact/interactions with the copper species is evident in directing the ORR towards a higher electron-transfer process.

The kinetic-limiting currents (j_k) were also calculated from the intercept of the fitted K-L plots at different potentials (Figures 8 and S6). As illustrated in Figure 8, the limiting currents measured on CMGr are 3 to 4 times higher than those of CM over the investigated potential range, showing again the positive effect of rGO. Furthermore, the j_k of CMGr is also significantly higher than the summed values of rGO [11] and CM, demonstrating that the interaction between the two phases goes beyond the superposition of the intrinsic response of rGO and Cu (sample CM) and that a copper-mediated process takes place (Figure 7b). For instance, limiting currents measured at -0.7 V were 14.5 (n = 3.7) and 13.7 mA/cm^2 (n= 3.9) for CMGr-sN and CMGr-sO, respectively. The values are about three times higher than those of rGO (ca. 5.10 mA/cm^2) determined under similar conditions [11]. These values are close to that measured on the Pt/C catalyst at our experimental conditions (Figure 7b), and even higher than those obtained for other Cu-based catalysts and some metal-free materials [9-11], despite our lower oxygen content, as above-mentioned, than that used when pure oxygen is used for

electrolyte saturation. This makes our catalysts even more promising, as their performance will be much increased under higher O_2 concentration in the electrolyte.

To further evaluate the suitability of these samples as ORR catalysts in an alkaline medium, the tolerance to methanol crossover was assessed at -0.34 V (Figure 9a). The chronoamperometry was first run under N_2 saturation of the electrolyte. When air was purged through the system a sharp increase in the cathodic current was observed for all samples. After stabilization of the current, three separate spikes of methanol were introduced into the testing cell and the current remained unchanged showing the high tolerance of these materials towards methanol oxidation. This tolerance is better than that on a Pt/C catalyst (commercial 20 wt. % Vulcan Pt/C), where some shift in current from cathodic to a reversed anodic has been found (Figure S9) [10, 27, 28].

The long-term stability of the electrocatalytic activity of the composites was also evaluated (Figure 9c) by applying 1000 potential cycles. After each 100 cycles the ORR current was determined as discussed below (-0.34 V for CM and at -0.34 V for CMGr). The data collected show a high stability of the electrodes with a slight performance attenuation for CMGr (9 %) after 1000 cycles. Furthermore, peak current values and peak potential shift are minimal, indicating that the catalysts studied present a good long-term stability. Stability tests were also performed by running the ORR for over 20 hours (Figure 9b) at a fixed potential; the data showed a similar response to that from the potential cycling mode, with a slight performance attenuation for CMGr (12%) and CM (15%). This confirms the high stability of the active centers of the prepared catalysts and the strong interactions between the metallic particles and the rGO, which prevent the loss of active sites during cycling. No leaching of copper was observed.

Summarizing, we show the superior activity performance of the copper/rGO composite for ORR in terms of the enhanced current density, low onset potential, high stability and superior methanol tolerance. To analyze the synergistic effect between the copper and rGO components, several aspects have to be considered related to the composition of our materials and chemical/structural transformations during their synthesis. The carbonization of copper containing MOF at a high temperature resulted in the synthesis of the catalyst with well-dispersed metallic species and rich redox chemistry, but showing a low activity for the electrochemical ORR. The incorporation of GO before the heat treatment resulted in the superior performance of CMGr for ORR, despite the slight clustering of the copper particles. The synthesis procedure applied and the reducing atmosphere provided during the thermal treatment let to the catalysts with similar textures/porosities and acidic/basic natures (Table 1). Thus the oxygen transfer to the surface active sites is expected to be comparatively fast in both cases, and cannot explain their different ORR activity. On the other hand, XPS data showed that the graphitic carbon was predominant in the Cu/rGO catalyst, as opposed to CM where the pyrolytic carbon was more abundant. This higher amount of the graphitic carbon in the former sample apparently increased the electric conductivity, which is one order of magnitude higher than that of the pyrolyzed MOF (2.6 S/m and 0.3 S/m for CMGr and CM, respectively). Moreover, the metallic copper particles are deposited on the relatively large graphene-based sheets enhancing the efficiency of the electron transfer processes. Both, metallic copper and graphene layers provide the local hydrophobic environment where oxygen “extracted” from water is attracted to the surface [50]. Then it accepts electrons through a direct path of a conducting support. The effects of the change of the water density in this hydrophobic nanospace can also affect this process [50]. Support for local hydrophobicity is in the XPS results discussed above (Figure 3 and Table 2).

Thus the combination of the specific physical, chemical and textural characteristics of CMGr (the presence of the conducting carbon phase, the well-dispersed copper particles and surface hydrophobicity) forms the unique surface architecture, where ability of dissolved oxygen to concentrate on the hydrophobic surface of CMGr at the local environment of the copper species, combined with the enhanced electron transfer properties of the rGO component on which these active copper centers are located (acting as a connector between the copper particles/atoms) would account for the superior electrocatalytic activity of CMGr compared to that of CM. For the latter, the oxygen and charge transfer processes are limited by the poor hydrophobicity (Table 1) and the low conductivity of the pyrolytic carbon phase (Table 3, Figure 3). This limits both, oxygen concentration on the surface and its ability to accept electrons.

Besides the catalytic activity, CMGr has also higher selectivity than CM as inferred from the higher number of electrons transfer (Figure 7b). Details on the nature of the intermediates formed would be needed to further discuss the differences in the mechanism of both catalysts. However, this is the subject of undergoing research and beyond the scope of this paper.

4. Conclusions

The results obtained show that, under appropriate stabilization conditions, Cu/rGO electrodes can be highly stable and active in electrocatalytic oxygen reduction in an alkaline medium. A thermal treatment of MOF/graphite oxide composite resulted in a hybrid material with a high metal loading. The unique spatial configuration of the copper atoms in the 3D framework of the pristine MOF and the separation of the small crystals by the graphene phase resulted in the relatively homogenous distribution of copper nanoparticles of small sizes assembled on the graphene sheets. These morphological features were not found on the surface of the carbonized MOF, even though the high dispersion of the reduced copper was detected there.

Owing to the combination of highly dispersed copper and the excellent electronic properties of rGO, the composites showed high electrocatalytic activity in ORR compared to the carbonized MOF. The stabilization of the composites under different conditions leads to the formation of different copper species with catalytic activity. The activity of the hybrid Cu/rGO material goes beyond the superposition of the performance of the individual components of the composite, demonstrating the synergistic effect of copper coupled to rGO. That synergy is linked to the enhanced conductivity and thus to the fast electron transfer caused by a direct contact of the dispersed copper metal nanoparticles with the conductive graphene-based phase. Moreover, hydrophobic sites created by this arrangement attract molecular oxygen dissolved in water. The current density values and limiting currents for CMGr outperform the values reported for Cu-based materials, and are close to the best performance reported for Pt and other metal-free electrocatalysts. The strong interactions between the copper atoms and rGO along with surface hydrophobicity favor the fast O_2 adsorption on the active sites and leads to the excellent electron transfer properties in the composites. Furthermore, the obtained materials showed excellent tolerance to methanol crossover and long term cycling stability after 20 hours. This new class of materials can replace the expensive platinum based catalyst and thus can contribute to the sustainability of our environment.

Acknowledgements

COA thanks the Spanish MECD for her Salvador de Madariaga mobility action (CTM2011/23378 and PRX12/00290).

Electronic Supplementary Information (ESI)

Characterization of the prepared materials by SEM/EDX, thermogravimetric analysis coupled to mass spectrometry, Koutecky–Levich (K-L) plots at different potential values, cyclic

voltammograms, linear sweep voltammograms and chronoamperometric response for 20 % Pt on Vulcan XC72 <5 nm and reduced graphite oxide.

References

1. B. C. H. Steele, A. Heinzel, Nature 414 (2001) 345-352.
2. D. S. Yu, E. Nagelli, F. Du, L. M. Dai, J. Phys. Chem. Lett. 1 (2010) 2165-2173.
3. J. D. Wiggins-Camacho, K. J. Stevenson, J. Phys. Chem. C 115 (2011) 20002-20010.
4. M. Lefevre, E. Proietti, F. Jaouen, J. P. Dodelet, Science 324 (2009) 71-74.
5. J. B. Xu, P. Gao, T. S. Zhao, Energy Environ. Sci. 5 (2012) 5333-5339.
6. I. Roche, E. Chainet, M. Chatenet, J. Vondrak, J. Phys. Chem. C 111 (2007) 1434-1443.
7. S. Guo, S. Zhang, S. Sun, Angew. Chem. Int. Ed. 52 (2013) 8526-8544; Angew. Chem. 125 (2013) 8686-8705.
8. H. Zhu, S. Zhang, Y.-X. Huang, L. Wu, S. Sun, Nano Lett. 13 (2013) 2947-2951.
9. R. Zhou, Y. Zheng, D. Hulicova-Jurcakova, S.Z. Qiao, J. Mater. Chem. A 1 (2013) 13179-13185.
10. J. Liang, Y. Jiao, M. Jaroniec, S.Z. Qiao, Angew. Chem. Int. Ed. 51 (2012) 11496-11500; Angew. Chem. 124 (2012) 11664-11668.
11. M. Seredych, T.J. Bandosz, Carbon 66 (2014) 227-233.
12. C. Zhu, S. Dong, Nanoscale 5 (2013) 1753-1767.
13. P. Kang, E. Bobyr, J. Dustman, K.O. Hodgson, B. Hedman, E.I. Solomon, T.D.P. Stack, Inorg. Chem. 49 (2010) 11030-11038.
14. Z. Chen, T.J. Meyer, Angew. Chem. Int. Ed. 52 (2013) 700-703; Angew. Chem. 125 (2013) 728-731.
15. Z. Chen, P. Kang, M.-T. Zhang, B.R. Stoner, T.J. Meyer, Energy Environ. Sci. 6 (2013) 813-817.

16. X.-Y. Yan, X.-L. Tong, Y.-F. Zhang, X.-D. Han, Y.-Y. Wang, G.-Q. Jin, Y. Qin, X.-Y. Guo, Chem. Commun. 48 (2012) 1892-1894.
17. E.I. Solomon, U.M. Sundaram, T.E. Machonkin, Chem. Rev. 96 (1996) 2563-2606.
18. J.A. Cracknell, K.A. Vincent, F.A. Armstrong, Chem. Rev. 108 (2008) 2439-2461.
19. M. Jahan , Z. Liu, K.P. Loh, Adv. Funct. Mater. 23 (2013) 5363-5372.
20. C. Petit, J. Burress, T.J. Bandosz, Carbon 49 (2011) 563-572.
21. C. Petit, B. Mendoza, T.J Bandosz, ChemPhysChem 11(2010) 3678-3684
22. C. Petit, B. Levasseur, B. Mendoza, T. J. Bandosz, Micro. Meso. Mat. 154 (2012) 107-112.
23. Y. Zhao, M. Seredych, Q. Zhong, T J. Bandosz, ACS Adv. 3, 9932-9941 (2013).
24. M.D. Allendorf, A. Schwartzberg, V. Stavila, A.A. Talin, Chem. Eur. J. 17 (2011) 11372-11388.
25. M. Jahan, Q.L. Bao, J.X. Yang, K.P. Loh, J. Am. Chem. Soc. 132 (2010) 14487-14495.
26. M. Jahan, Q. Bao, K. P. Loh, J. Am. Chem. Soc. 134 (2012) 6707-6713.
27. S. Yang, L. Zhi, K. Tang, X. Feng, J. Maier, K. Mullen, Adv. Funct. Mater. 22 (2012) 3634-3640.
28. J. Liang, Y. Zheng, J. Chen, J. Liu, D. Hulicova-Jurcakova, M. Jaroniec, S.Z. Qiao, Angew. Chem. Int. Ed. 51 (2012) 3892-3896; Angew. Chem. 124 (2012) 3958-3962.
29. S. Ma, G.A. Goenaga, A.V. Call, D.-J. Liu, Chem. Eur. J. 17 (2011) 2063-2067.
30. S. S.-Y. Chui, S. M.-F. Lo, J. P. H. Charmant, G. Orpen, I. D. Williams, Science 283 (1999) 1148-1150.
31. M.M. Dubinin, in: P.L. Walker (Ed.), Chemistry and Physics of Carbon, Marcel Dekker, New York, USA, Vol. 2, 1966, pp. 51-120.
32. J.F. Moulder, W.F. Stickle, P.E. Sobol, K.D. Bomben, Standard Spectra for Identification and Interpretation of XPS data, Perkin Elmer, Eden Prairie, MN, 1992.

33. S. Poulston, P.M. Parlett, P. Stone, M. Bowker, Surf. Interface Anal. 24 (1996) 811-820.

34. M.R. Johan, M.S.M. Suan1, N.L. Hawari, H.A. Ching, Int. J. Electrochem. Sci. 6 (2011) 6094 -6104.

35. C. Petit, M. Seredych, T.J. Bandosz, J. Mater. Chem. 19 (2009) 9176-9185.

36. S.H. Huh, in: S. Mikhailov (Ed.), Physics and Applications of Graphene – Experiments, InTech, 2011, pp. 73-90.

37. C. Moreno-Castilla, F.J. Maldonado-Hódar, J. Rivera-Utrilla, E. Rodríguez-Castellón, Appl. Catal. A: Gen. 183 (1999) 345-356.

38. A.P. Terzyk, Colloids Surf. A: Physicochem. Eng. Asp. 177 (2001) 23-45.

39. D. Popovici, J.E. Klemberg-Sapieha, G. Czeremuszkin, E. Sacher, M. Meunier, L. Martinu, Microelectron. Eng. 33 (1997) 217-221.

40. C.D. Wagner, A.V. Naumkin, A. Kraut-Vass, J.W. Allison, C.J. Powell, J.R.Jr. Rumble, NIST Standard Reference Database 20, Version 3.4, http:/srdata.nist.gov/xps/, 2003.

41. E. Moretti, M. Lenarda, P. Riello, L. Storaro, A. Talon, R. Frattina, A. Reyes-Carmona, A. Jiménez-López, E. Rodríguez-Castellón, Appl. Catal. B: Environ. 129 (2013) 556-565.

42. C. Petit, B. Mendoza, T.J. Bandosz, Langmuir 26 (2010) 15302-15309.

43. M. Seredych, J.C. Idrobo, T.J. Bandosz, J. Mater. Chem. A 1 (2013) 7059-7067.

44. M. Jayalakshmi, K. Balasubramanian, Int. J. Electrochem. Sci. 3 (2008) 1277-1287.

45. J.M.M. Droog, C.A. Alderliesten, P.T. Alderliesten, G.A. Bootsma, J. Electroanal. Chem. Interfacial Electrochem. 111 (1980) 61-70.

46. Y. Wan, X. Wang, H. Sun, Y. Li, K. Zhang, Y. Wu, Int. J. Electrochem. Sci. 7 (2012) 7902-7914.

47. F.H. Assaf, A.M. Zaky, S. S. Abd EI-Rehim, Appl. Surf. Sci. 187 (2002) 18-27.

48. J. Qiao, L. Xu, L. Ding, P. Shi, L. Zhang, R. Baker, J. Zhang, Int. J. Electrochem. Sci. 8 (2013) 1189-1208.

49. Z. Lin, G. Waller, Y. Liu, M. Liu, C.-P. Wong, Adv. Energy Mater. 2 (2012) 884-888.

50. D. A. Doshi, E. B. Watkins, J. N. Israelachvili, J. Majewski, PNAS 102 (2005) 9458-9462.

Captions to the Tables

Table 1. The parameters of porous structure calculated from nitrogen adsorption isotherms at -196 ºC, number of total acidic groups determined by potentiometric titration, surface pH and hydrophobicity level.

Table 2. Atomic concentration (%) of elements on the surfaces of CMGr and CM determined by XPS.

Table 3. Relative distribution of surface functional groups identified by XPS.

Captions to the Figures

Figure 1. Texture characterization of the materials studied: a-d) SEM; and e-l) TEM images, respectively.

Figure 2. X-Ray diffraction patterns for the materials studied.

Figure 3. C1s, Cu 2p and O1s core level peaks of XPS spectra for the synthesized samples.

Figure 4. a) Example of the stabilization of CM and CMGr under oxygen saturation of the electrolyte (the arrows indicate increasing intensity with the number of cycles); b) Cyclic voltamograms of the electrodes after stabilization under O_2 (-sO) and N_2 (-sN) saturation of the electrolyte (0.1 M KOH). Electrodes are pasted on Ti foil collectors.

Figure 5. O_2 consumption during ORR on CM and CMGr under controlled O_2 concentration in the electrolyte.

Figure 6. a) Linear sweep voltammograms with indication of the graphical calculation of the ORR onset potential (inset), and b) cyclic voltammograms on modified glassy carbon RDE in air-saturated 0.1 M KOH at different rotation speeds at scan rate of 5 mV/s in the different stabilization conditions. Inset: indication of the ORR activity of CMGr-sO, for clarity.

Figure 7. a) Linear sweep voltammograms on the modified glassy carbon RDE in air-saturated 0.1 M KOH at 2000 rpm and scan rate of 5 mV/s for the materials studied compared to rGO (reintroduced from reference [11]) and 20% Pt on Vulcan XC72; b) Kinetic-limiting

current and number of electron transfer for rGO and CM-sO at -0.4 V and for CMGr-sO and 20% Pt on Vulcan XC72 at -0.34 V.

Figure 8. a) Koutecky–Levich (K-L) plots for the materials studied at -0.4 V (for CMGr with O_2 K-L plot presented at -0.34 V); b) Number of electron transfer versus potential.

Figure 9. a) Chronoamperometry for methanol tolerance, and long term stability of the catalysts (b) after 20 hours at -0.34V and (c) after 1000 potential cycles.

Table 1. The parameters of porous structure calculated from nitrogen adsorption isotherms at -196 ºC, number of total acidic groups determined by potentiometric titration, surface pH and hydrophobicity level.

Sample	S_{BET} (m^2/g)	V_t (cm^3/g)	V_{meso} (cm^3/g)	V_{mic}(DA) (cm^3/g)	Total acidic groups (mmol/g)	pH	HL
CM	117	0.135	0.077	0.058	ND	8.21	0. 29
CMGr	53	0.103	0.077	0.026	0.287	7.76	0.66

ND- not detected.

Table 2. Atomic concentration (%) of elements on the surfaces of CMGr and CM determined by XPS.

Sample	C 1*s*	O 1*s*	N 1*s*	F 1*s*	Cu 2*p*
CMGr	74.77	3.62	0.71	22.64	0.61
CM	64.00	5.21	0.50	29.01	1.23

Table 3. Relative distribution of surface functional groups identified by XPS.

	CMGr	CM
Copper carbide	1.76	---
C-C (pyrolytic carbon- 284.3 eV)	---	28.58
C-C (graphitic carbon in sp^2 configurations - 284.8 eV)	49.95	6.99
C-O (phenolic, alcoholic, etheric – 286.0-286.1eV) and -CH_2- of PVDF	19.65	22.83
C=O (carbonyl or quinone - 287.0 eV)	8.69	11.32
O-C=O (carboxyl or ester – 288.2-288.4 eV)	3.61	4.36
-CF_2- (290.6 eV) of PVDF	16.72	25.92
Oxygen/OH^- anion (in metal oxides - 530.8 eV)	19	33
O=C (in carboxyl/carbonyl-531.7 eV)	42	41
O-C (in phenol/epoxy– 533.5-533.8 eV)	39	26

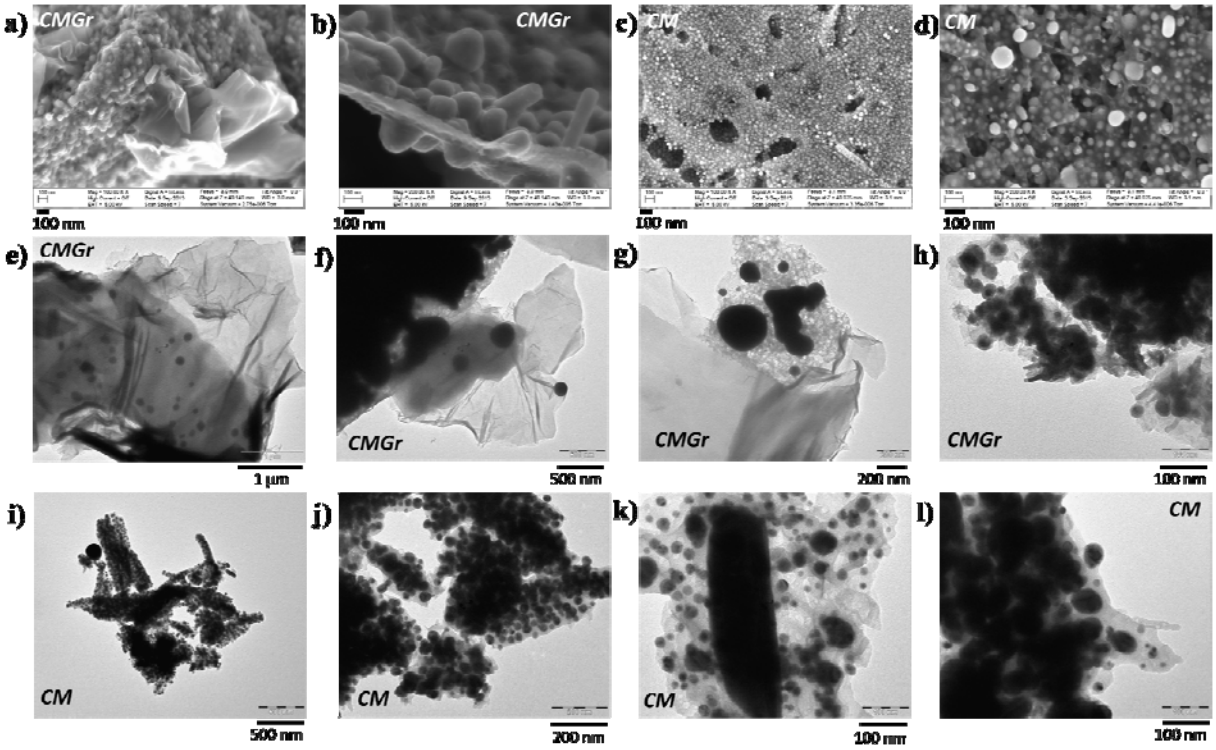

Figure 1. Texture characterization of the materials studied: a-d) SEM; and e-l) TEM images, respectively.

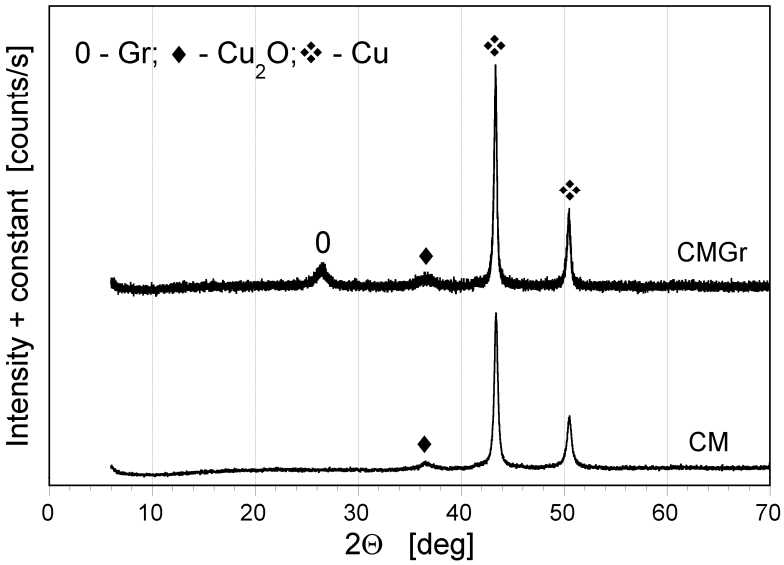

Figure 2. X-Ray diffraction patterns for the materials studied.

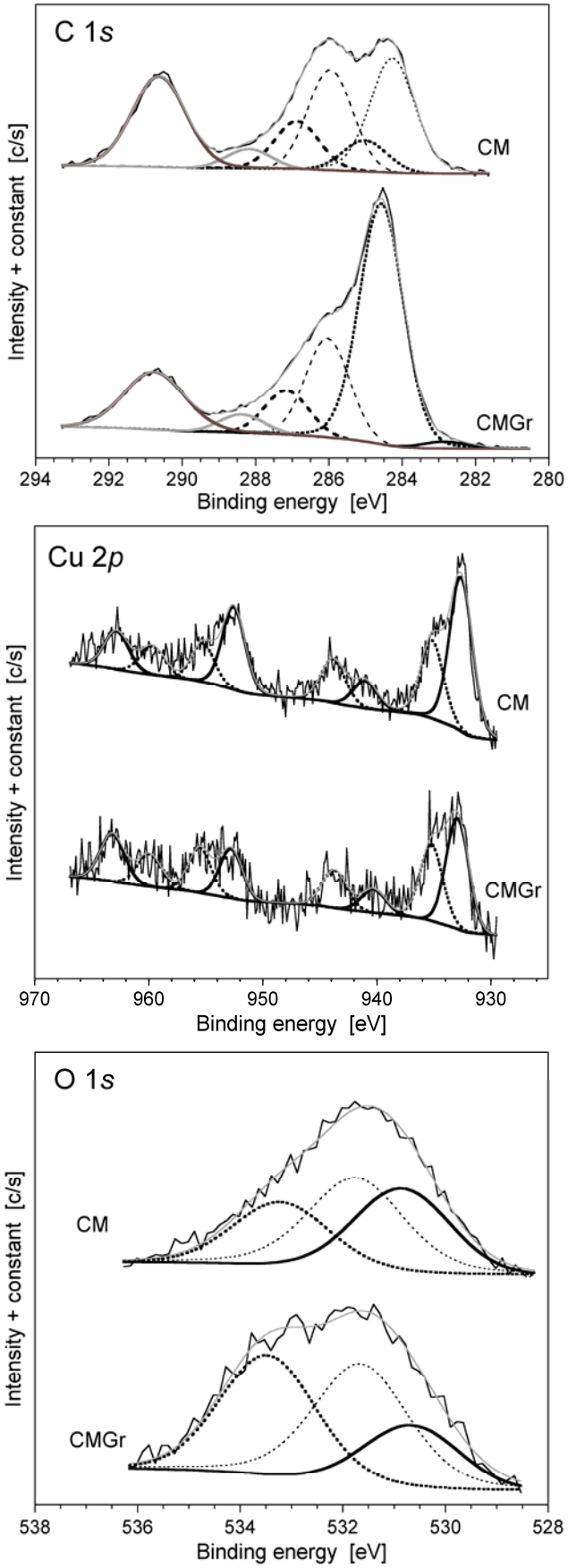

Figure 3. C1s, Cu 2p and O1s core level peaks of XPS spectra for the synthesized samples.

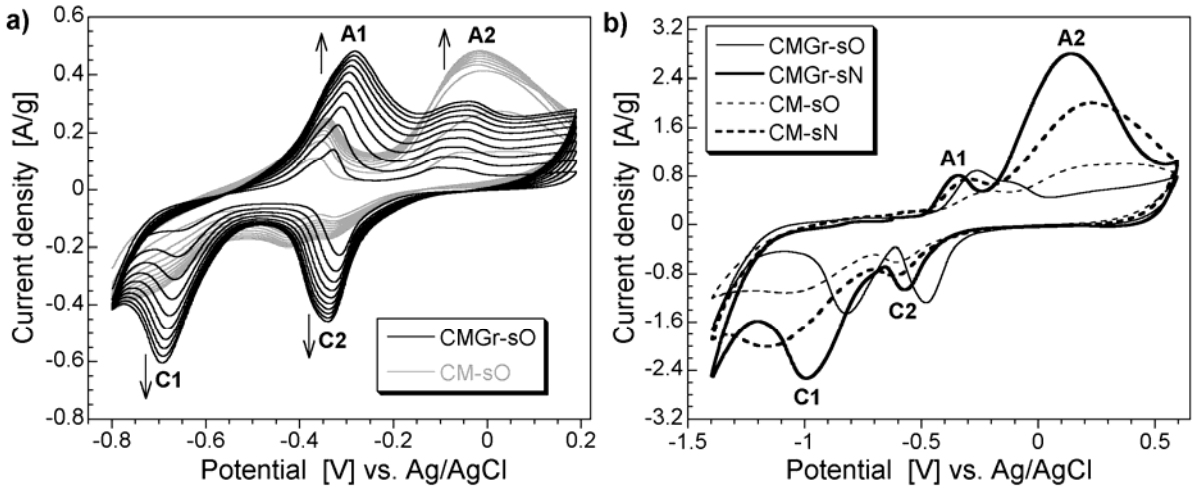

Figure 4. a) Example of the stabilization of CM and CMGr under oxygen saturation of the electrolyte (the arrows indicate increasing intensity with the number of cycles); b) Cyclic voltamograms of the electrodes after stabilization under O_2 (-sO) and N_2 (-sN) saturation of the electrolyte (0.1 M KOH). Electrodes are pasted on Ti foil collectors.

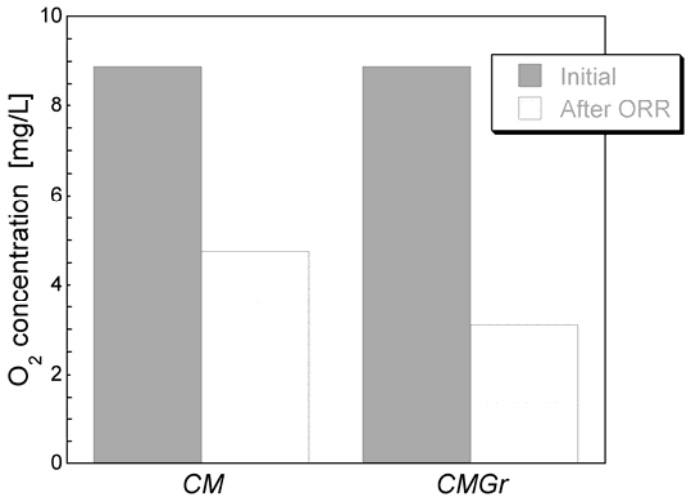

Figure 5. O_2 consumption during ORR on CM and CMGr under controlled O_2 concentration in the electrolyte.

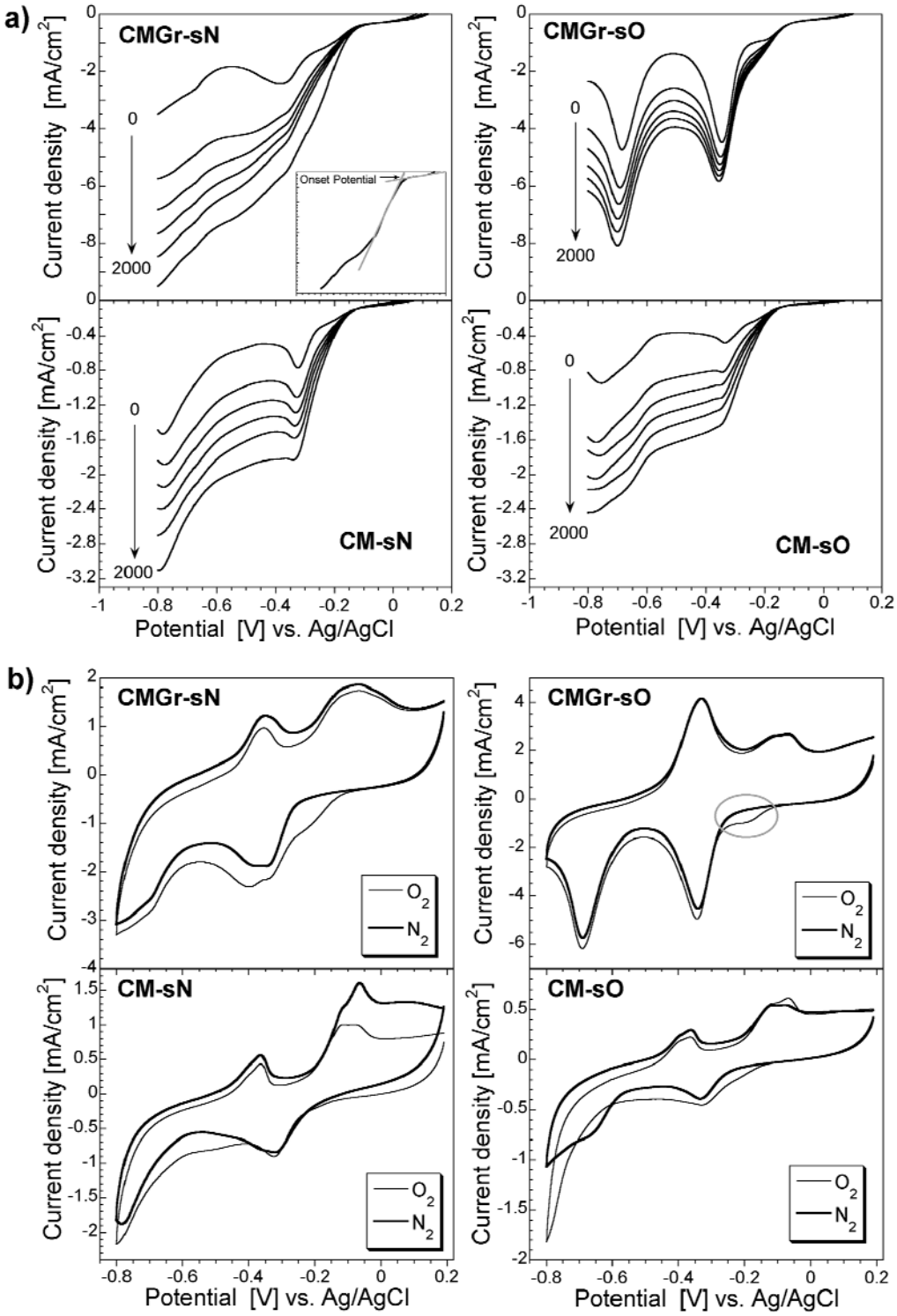

Figure 6. a) Linear sweep voltammograms with indication of the graphical calculation of the ORR onset potential (inset), and b) cyclic voltammograms on modified glassy carbon RDE in air-saturated 0.1 M KOH at different rotation speeds at scan rate of 5 mV/s in the different stabilization conditions. Inset: indication of the ORR activity of CMGr-sO, for clarity.

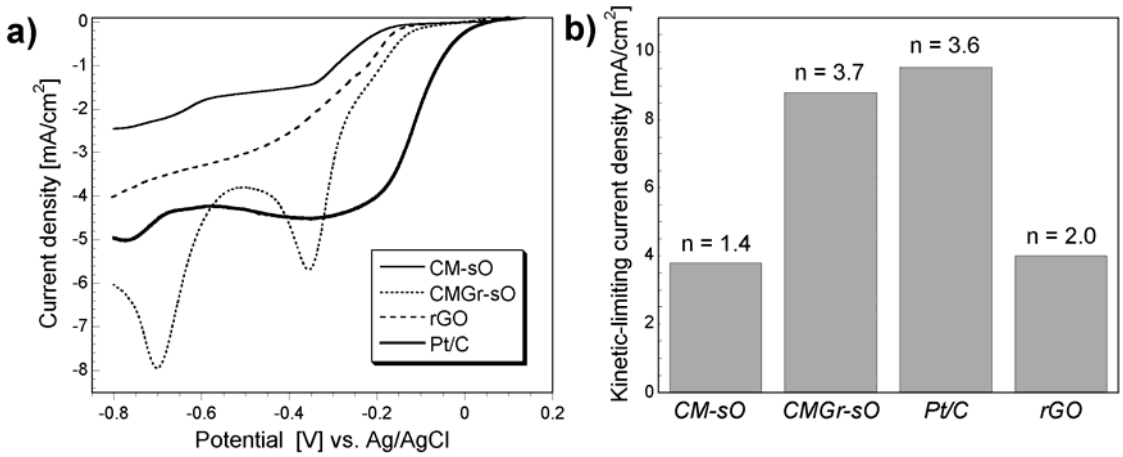

Figure 7. a) Linear sweep voltammograms on the modified glassy carbon RDE in air-saturated 0.1 M KOH at 2000 rpm and scan rate of 5 mV/s for the materials studied compared to rGO (reintroduced from reference [11]) and 20% Pt on Vulcan XC72; b) Kinetic-limiting current and number of electron transfer for rGO and CM-sO at -0.4 V and for CMGr-sO and 20% Pt on Vulcan XC72 at -0.34 V.

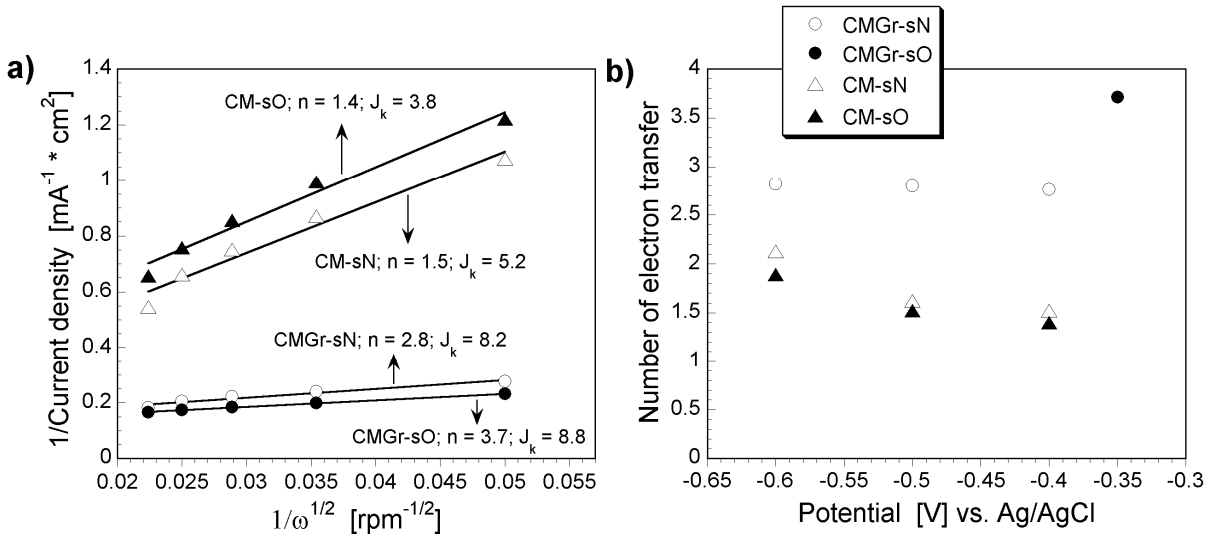

Figure 8. a) Koutecky–Levich (K-L) plots for the materials studied at -0.4 V (for CMGr with O_2 K-L plot presented at -0.34 V); b) Number of electron transfer versus potential.

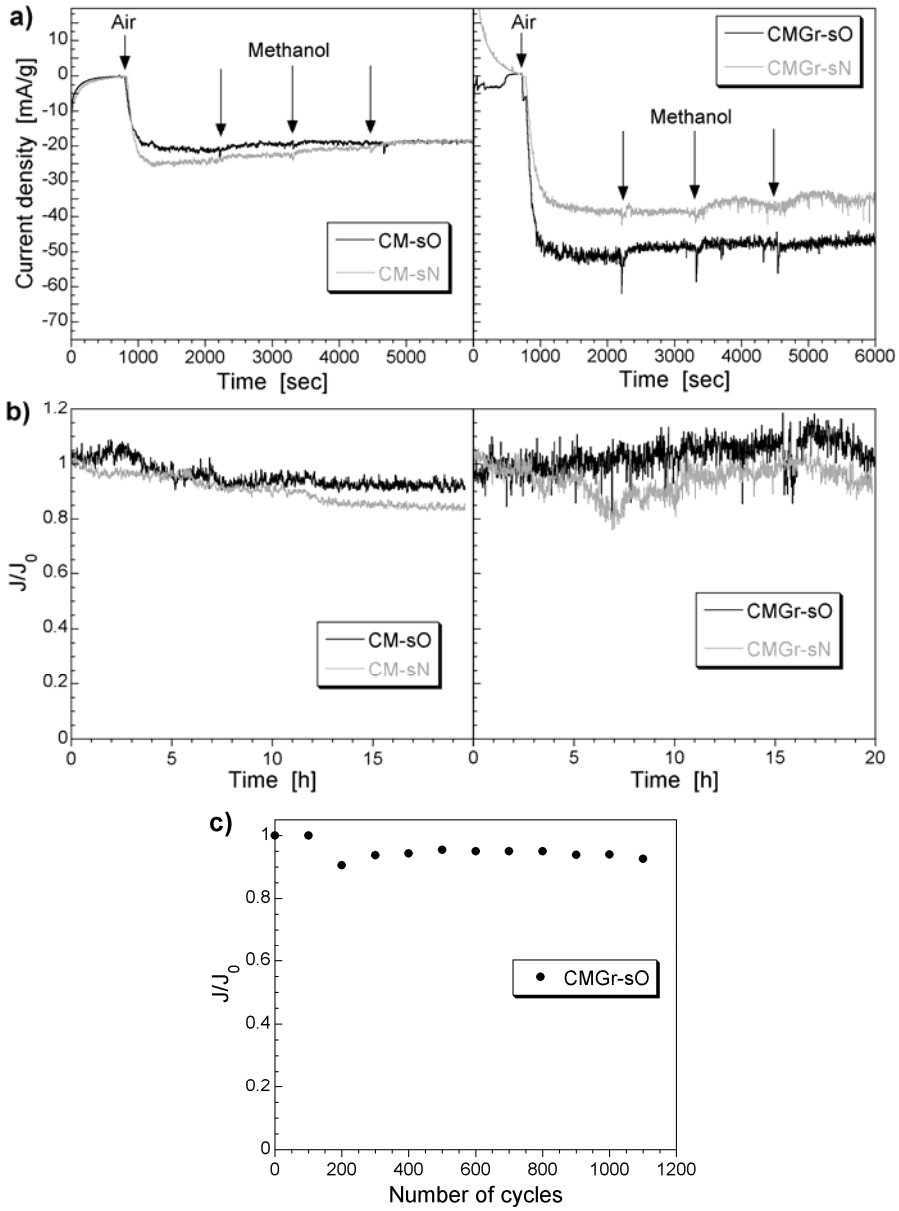

Figure 9. a) Chronoamperometry for methanol tolerance, and long term stability of the catalysts (b) after 20 hours at -0.34V and (c) after 1000 potential cycles.

SUPPLEMENTARY INFORMATION

New copper/GO based material as an efficient oxygen reduction catalyst in alkaline medium: The role of unique Cu/rGO architecture

Conchi O. Ania[2], Mykola Seredych[1], Enrique Rodriguez-Castellon[3], and Teresa J. Bandosz[1*]

[1]The City College of New York

160 Convent Avenue, New York, NY 10031 (USA)

[2]Dpt. Chemical Processes in Energy and Environment, Instituto Nacional del Carbón (INCAR, CSIC), C/ Francisco Pintado Fe 26, Oviedo 33011 (Spain)

[3]Dept. De Quimica Inorganica, Universidad de Malaga (Spain)

[*]Corresponding author. Tel: (212) 650-6017; Fax: (212) 650-6107; E-mail address: tbandosz@ccny.cuny.edu (T.J. Bandosz)

1. Experimental Details

1.1. Thermal analysis-mass spectroscopy (TA-MS)

Thermogravimetric (TG) curves were obtained using a TA instrument thermal analyzer (SDT Q 600), which was connected to a gas analysis system (OMNI Star^{TM}) mass spectrometer. The samples were heated up to 1000 ^{o}C (10 ^{o}C/min) under a constant helium flow (100 mL/min). From the TG curves, differential TG (DTG) curves were derived. The composition of gases was evaluated by MS and gas evolution profiles as a function of temperature were obtained.

1.2. Potentiometric titration

Potentiometric titration measurements were performed with a 888 Titrando automatic titrator (Metrohm). The instrument was set at the mode where the equilibrium pH is collected. Subsamples of the initial materials (~ 0.050 g) were added to $NaNO_3$ (0.01 M, 25 mL) and placed in a container maintained at 25 ^{o}C overnight for equilibrium. During the titration the suspension was continuously saturated with N_2 to eliminate the influence of atmospheric CO_2. The suspension was stirred throughout the measurements. Volumetric standard NaOH (0.1 M) was used as the titrant starting from the initial pH of the materials suspension up to pH 11. The experimental data was transformed into a proton binding curves, Q, representing the total amount of protonated sites [S1, S2].

1.3. Determination of number of electron transfer and kinetic-limiting current.

The Koutecky–Levich (K-L) equation was used to calculate the number of electron transfer and kinetic-limiting current at the different potential values from linear sweep voltammetry (LSV) [S3].

$$\frac{1}{j} = \frac{1}{j_k} + \frac{1}{j_D} = \frac{1}{j_k} + \frac{1}{0.2nFAC_{O_2}D_{O_2}^{2/3}\nu^{-1/6}\omega^{1/2}}$$

where j, j_k and j_D are the measured current density, the kinetic-limiting current density and the diffusion-limiting current density, respectively; n is the number of electrons; F is the Faraday

constant (96487 C/mol); A is the electrode area, C_{O2} is the oxygen concentration (1.2 x 10^{-6} mol/cm^3); D_{O2} is the diffusion coefficient of O_2 in the electrolyte (1.9 x10^{-5} cm^2/s); ν is the kinematic viscosity of the electrolyte (0.01 cm^2/s); ω is the rotation speed in rpm. 0.2 is a constant when the rotation speed is in rpm. The number of electrons transferred per oxygen molecule during ORR was calculated from the slope of the plot $1/j_k$ vs. $\omega^{-1/2}$. The kinetic-limiting currents calculated from the intercept of the fitted K-L plots at different potentials.

References

S1. J. Jagiello, Langmuir 10 (1994) 2778-2785.

S2. J. Jagiello, T.J. Bandosz, J.A. Schwarz, Carbon 32 (1994) 1026-1028.

S3. C. Song, J. Zhang, in: J, (Ed.), PEM Fuel Cell Electrocatalysts and Catalysts Layers: Fundamentals and Applications, Springer, Vol. XXII, 2008, pp. 89-134.

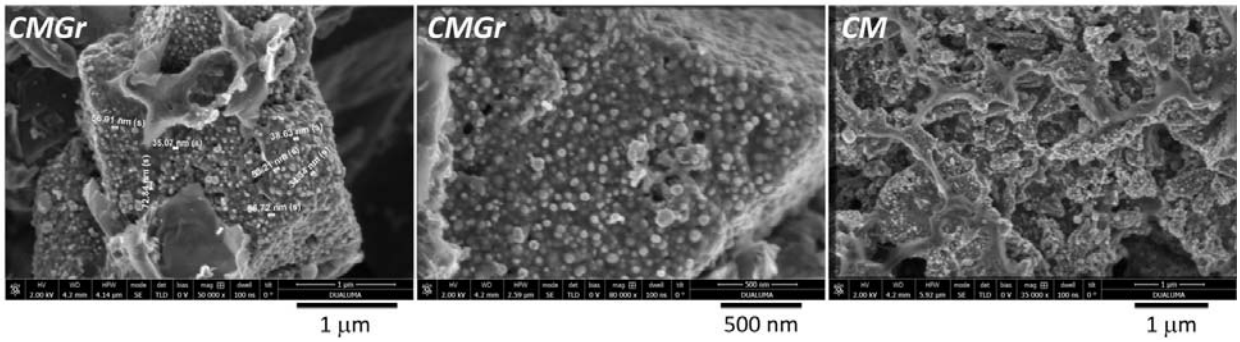

Figure S1. SEM images of the synthesized samples at different magnifications.

Table S1. Semiquantitative analysis of surface chemistry (from five different spots on each micrographs in at. %).

Sample	C ± σ	O ± σ	F ± σ	Cu ± σ
CMGr	70.0 ± 19	4.1 ± 3.5	1.9 ± 1.7	23.5 ± 17.2
CM	58.2 ±10.5	3.9 ± 0.6	0.9 ± 0.3	37.0 ± 11.2

The specific micrographs are those:

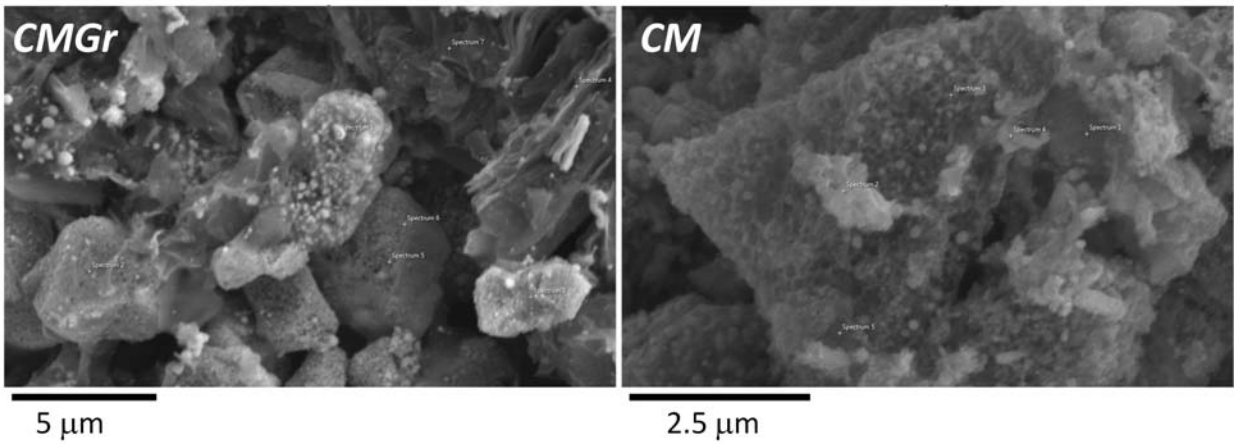

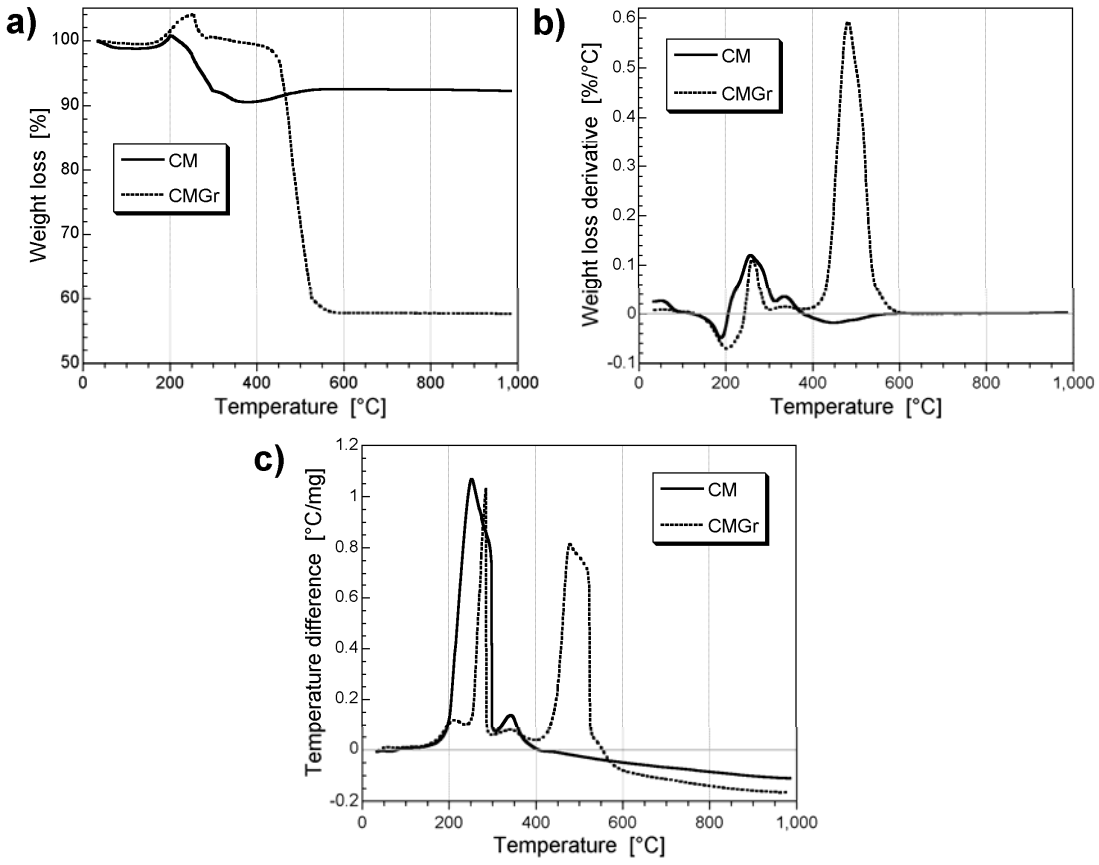

Figure S2. a) Thermal Gravimetry (TG) curves; b) Differential Thermal Gravimetry (DTG) curves and c) Differential Thermal Analysis (DTA) curves in air for the materials studied.

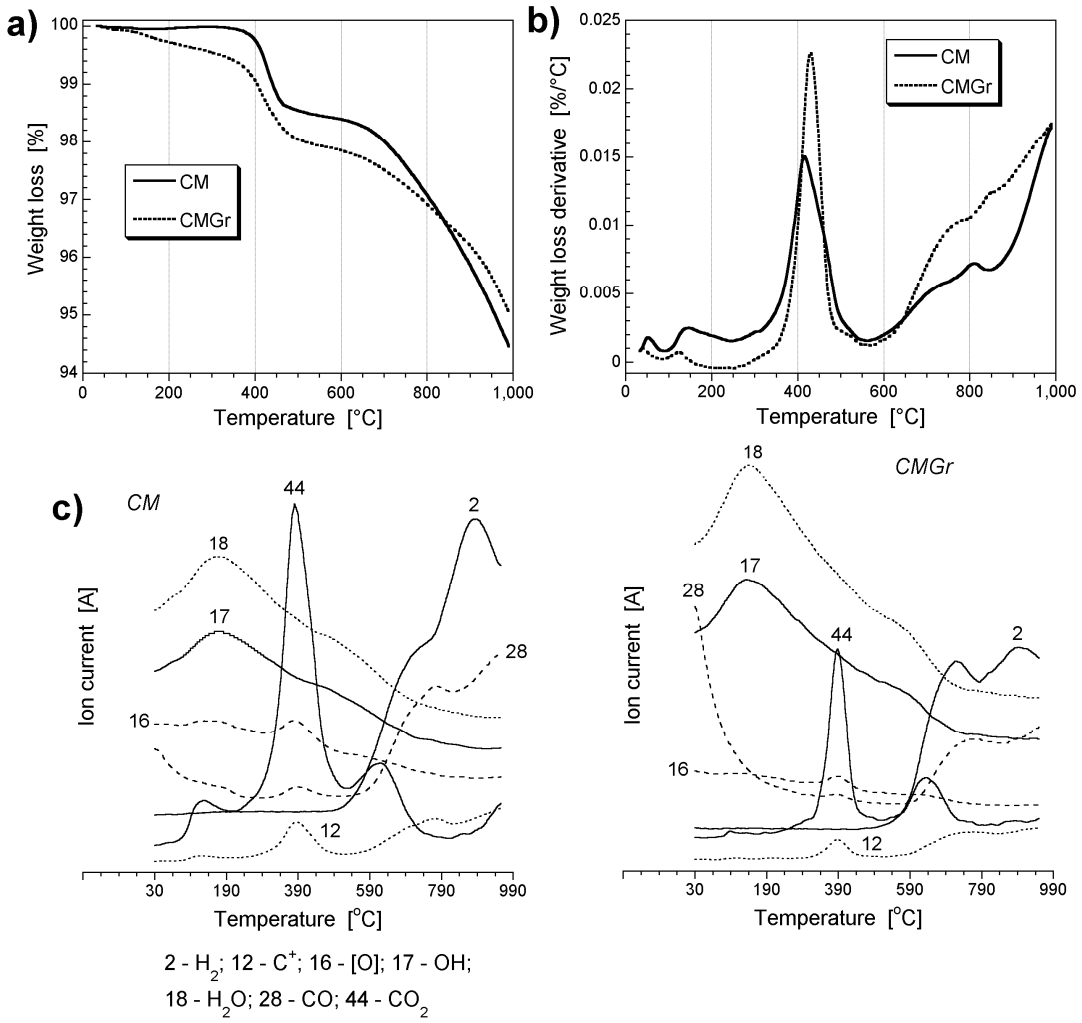

Figure S3. a) TG curves; b) DTG curves in helium and c) the MS patterns (multiplication factor: MW-2 x 1; MW-12 x 30; MW-16 x 7; MW-17 x 5; MW-18 x 1.7; MW-28 x 2; MW-44 x 8).

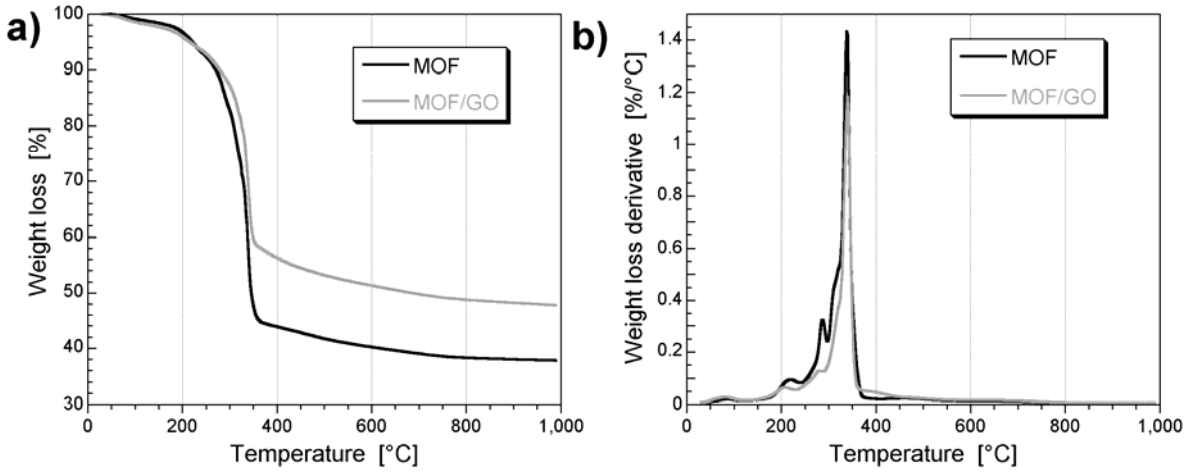

Figure S4. a) Thermal Gravimetry (TG) curves; b) Differential Thermal Gravimetry (DTG) curves in nitrogen for the initial MOF and MOF/GO composite used as catalysts precursors.

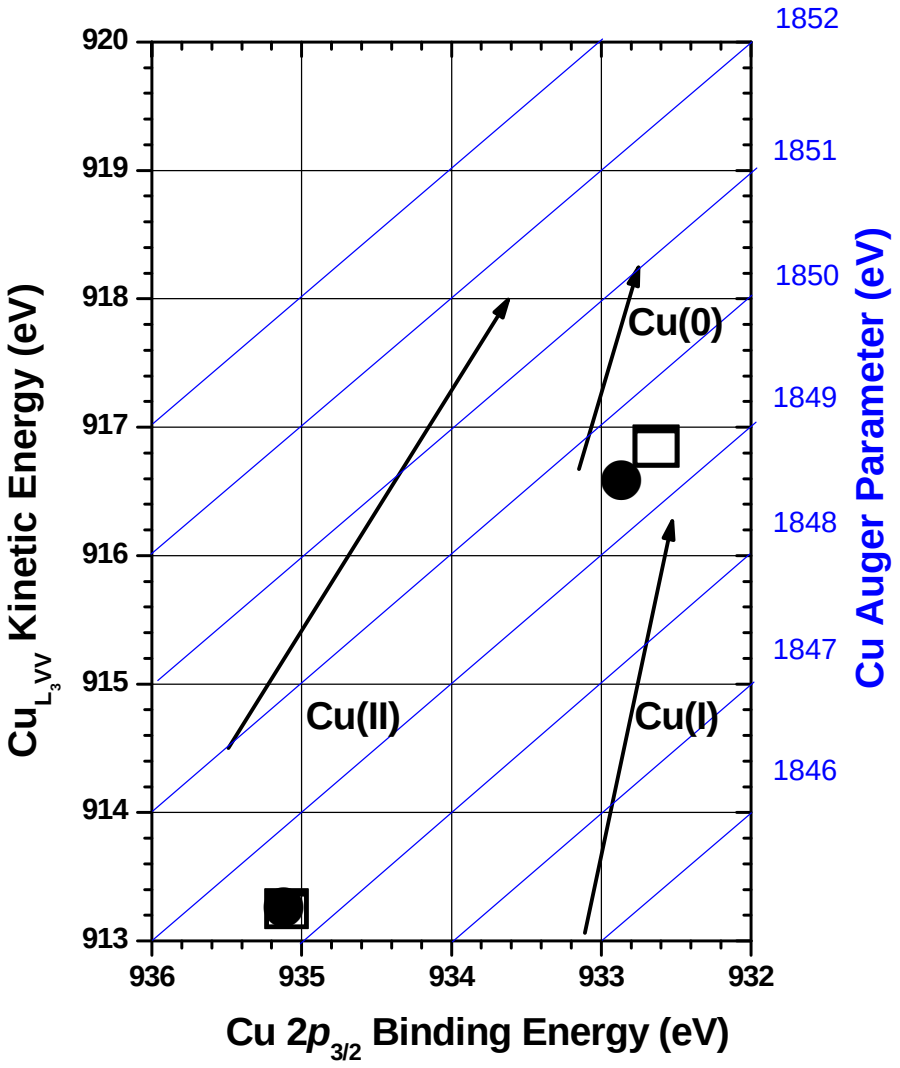

Fig. S5. Wagner plot for the samples CMGr (●) and CM (□). The arrows represent the typical dependence for Cu(0), Cu(I) and Cu(II).

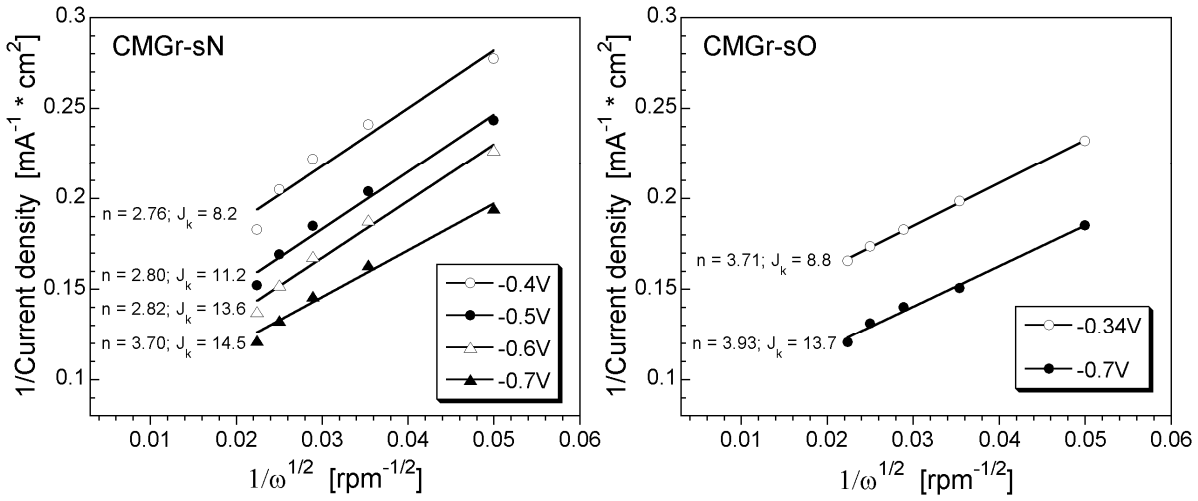

Figure S6. Koutecky–Levich (K-L) plots for the materials studied at different potential values.

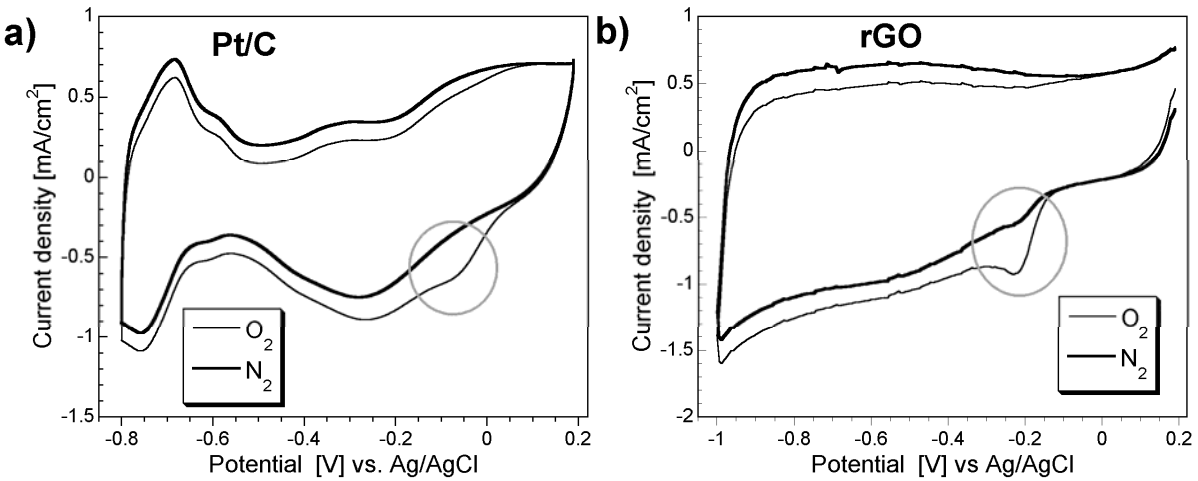

Figure S7. Cyclic voltammograms on modified glassy carbon RDE in air-saturated 0.1 M KOH at scan rate of 5 mV/s: a) for 20% Pt on Vulcan XC72 <5 nm (Pt); b) data for the reduced graphite oxide reintroduced from Reference [11]. Inset: indication of the ORR activity.

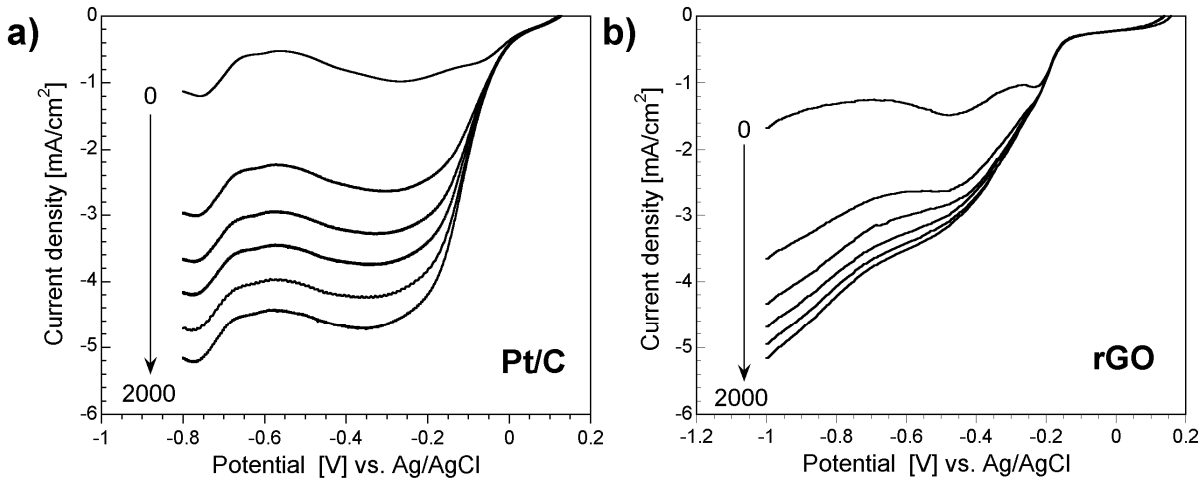

Figure S8. Linear sweep voltammograms on the modified glassy carbon RDE in air-saturated 0.1 M KOH at different rotation speeds at the scan rate of 5 mV/s: a) for 20% Pt on Vulcan XC-72; b) data for the reduced graphite oxide reintroduced from Reference [11].

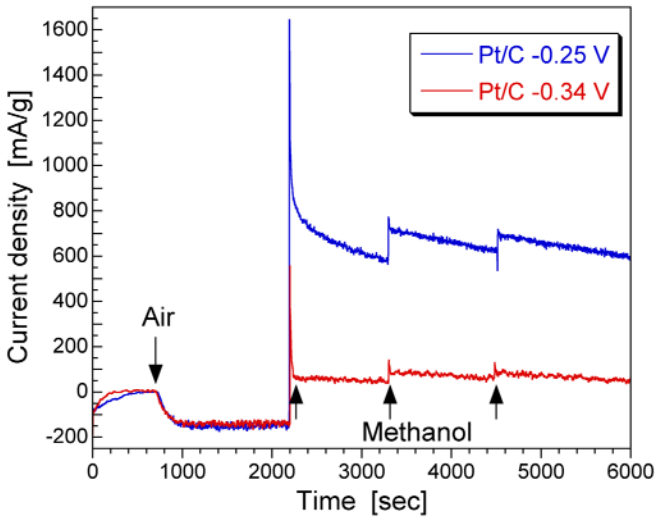

Figure S9. Chronoamperometric response for 20% Pt on Vulcan XC-72 at -0.25 V and -0.34 V.